Verification and measurement of the near-field radiatio75heat transfer properties and thermal sensing of a gradient metamaterial

MIN ZHONG*
Hezhou University, 542899, Hezhou, China

In recent years, metamaterials have gradually been applied in the field of near-field radiation heat transfer sensing. Here, the near-field radiation performance of a tunable metamaterial was verified and optimized in the range of 0.5-4.0THz. The coupling effect between the LSP mode distributed on the surface of nanogradient particles and the SPP mode on the surface of the metal structure improves the near-field radiation performance of this metamaterial structure. The near-field radiation performance is determined by the gradient factor and filling factor of gradient nanoparticles. This gradient metamaterial was applied to the thermal performance sensing scheme of fabric samples. The thickness and type of fabric samples are central Asian factors affecting thermal performance. These measurement results provide a foundation for expanding the application of gradient metamaterials.

(Received February 17, 2025; accepted October 14, 2025)

Keywords: Metamaterials, Dirac semimetal, Fabric samples, Weyl semimetal, Gradient material, Near-field radiation heat transfer

1. Introduction

In recent years, artificially prepared metamaterials/metasurfaces have been reported by an increasing number of researchers [1-4]. Many interesting resonant behaviors are acquired by these structures [5-8]. Numerous optoelectronic devices based on metamaterials/metasurfaces have been verified and applied [9-12]. In addition, to expand the properties of these metamaterials/metasurface surfaces, many interesting medium layers have been widely applied in structural design, such as VO2, liquid crystals, GST, etc. [13-16]. Currently, these reported metamaterials/metasurfaces are mainly applied in multiple industrial fields, such as sensing. However, during the application process, the impact of near-field radiant heat transfer (NFRHT) of these devices on performance has been discovered and valued by researchers [17-18]. Based on functional devices (NFRHT), many interesting optoelectronic devices have been proposed and verified by researchers, such as thermal management, thermophotovoltaic, logic gates, etc. [19-22]. To expand the NFRHT performance of photoelectric equipment, two methods have been applied in the industrial field. On the one hand, the design of the Wiener structure is optimized to enhance the performance of NFRHT [23-26]. On the other hand, tunable media are applied to the structural strategy of optoelectronic equipment to achieve the modulation of NFRHT performance [27-30].

In recent years, a third strategy for enhancing the NFRHT performance of optoelectronic devices has been confirmed by researchers. Applying gradient dielectric materials to the structural strategy of optoelectronic equipment can effectively enhance the performance of NFRHT. Regrettably, this strategy mainly achieves the corresponding functions by stacking gradient materials, which is not conducive to industrial applications. Therefore, in order to expand the industrial application of gradient metamaterials, a strategy of using gradient nanoparticles to enhance the performance of NFRHT has been proposed and verified. Such a structural strategy is different from the reported results [19-22]. Specifically, here, gradient nanoparticles are uniformly distributed in the medium layer, and then the performance enhancement of NFRHT is achieved by optimizing the gradient factor and filling factor. The measurement results verified the effectiveness of this structural strategy. These measurement results make it possible to develop new types of optoelectronic devices.

2. Structure and sample

Fig. 1 (a) shows the proposed structural strategy, which consists of five layers of materials: Dirac semimetal layer, SU-8+Gradient nanoparticles, GST layer, Weyl semimetal layer, and SiO2 layer. The geometric parameters of this structure are as follows: lattice constant P=10 micrometers, diameter d=5

micrometers, and thickness h1=1.0 micrometers, h2=20.0 micrometers, h3=10.0 micrometers, h4=4.0 micrometers, h5=8.0 micrometers. All the simulation results were obtained using the software HFSS. During the modeling process, ideal electromagnetic boundaries and perfectly matched layers are adopted as boundary conditions to eliminate the scattering loss of electromagnetic waves. The size of the grid is automatically matched by the system. The basic properties of the materials are also automatically matched by the simulation system without the need for manual input. The excitation port is located 10 microns directly above the structure, and the receiving port is located 8 microns below. The step size of the scanning frequency is 0.001THz.

The preparation steps of the sample are as follows: (a) A 2mm thick glass is used as a temporary substrate. A 1mm thick SU-8 is covered on the glass plate by a spinner (MSC-400Bz-6N spinner), and the SU-8 is layer cured by a hot plate. (b) Fix the temporary substrate inside the vacuum coating machine (ZZL-U400C) and cover the SU-8 table main with a layer of SiO2. (c) Use acetone to remove the SiO2 layer such as SU-8. (d) Fix the SiO2 layer inside the vacuum coating machine (ZZL-U400C) and cover the surface of the SiO2 layer with a layer of Weyl semimetal. (e) The GST layer was covered on the surface of the Weyl semimetal layer by using a vacuum coating machine (ZZL-U400C). (f) A layer of SU-8+Gradient nanoparticles was applied to the surface of GST using a glue spinner and cured with a hot plate. (g) The Dirac semi-metal layer was covered on the surface of SU-8 by a vacuum coating machine (ZZL-U400C), and the disc array was defined on the Dirac semi-metal layer by an etching machine. (h) The optical photograph of the sample is shown in Fig. 1 (b). The NFRHT properties of the samples were obtained using the Radiation Flux Meter.

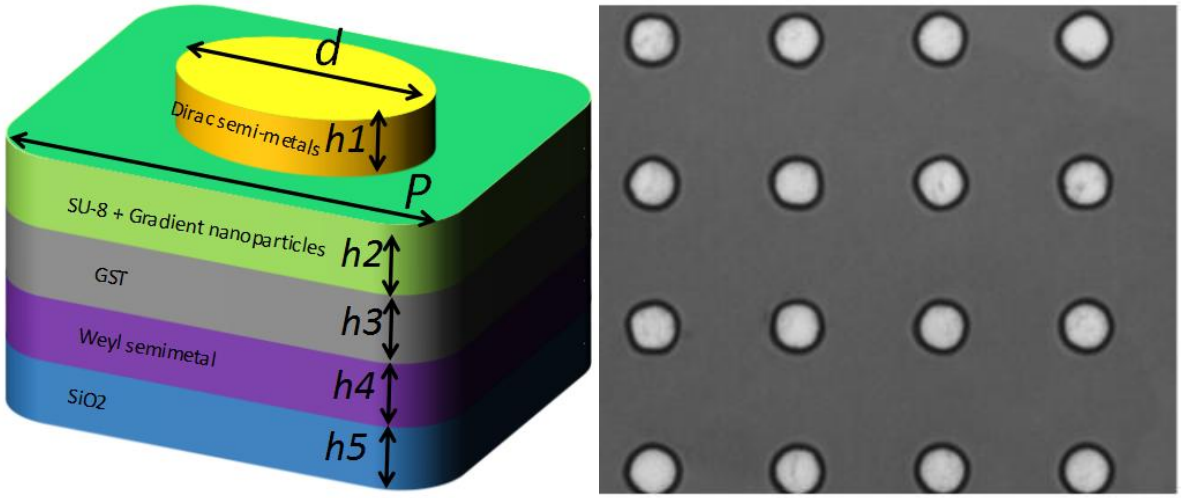

(a) *(b)*

Fig. 1. (a) Three-dimensional diagram. (b) Optical photographs of the sample (colour online)

The NFRHT performance measurement results and simulation results of this metamaterial sample are presented in Fig. 2 (a). In the experiment, the specific parameters of the gradient nanoparticles are: n=0.55, f=0.03. Within the range of 0.5-4.0THz, there are three near-field radiation peaks, with the resonance points being 1.782THz, 3.521THz, and 3.633THz, and the intensities being 6.52, 5.68, and 6.11. Fig. 2 (a) also presents the corresponding simulation results, with the resonance points being 1.784THz, 3.520THz, and 3.626THz, and the intensities being 6.88, 5.56, and 6.15. Among them, the radiation peak at 1.782THz is based on the LSP mode resonance, while those at 3.520THz and 3.626THz are based on the SPP mode resonance. In the second set of experiments, the gradient nanoparticles were removed, and the near-field radiation properties of the metamaterial were measured and simulated, as shown in Fig. 2 (b). In the experiment, the geometric parameters of the metamaterial remained unchanged. In the range of 0.5-4.0HTz, two near-field radiation peaks were observed, with resonance points of 1.788THz and 3.621THz, and intensities of 1.62 and 1.48. The simulation results are basically consistent with the measurement results, as shown in Fig. 2 (b). By comparing the results in Fig. 2 (a) and Fig. 2 (b), it can be seen that incorporating gradient nanoparticles into the structural strategy can significantly improve the near-field radiation performance of this metamaterial sample.

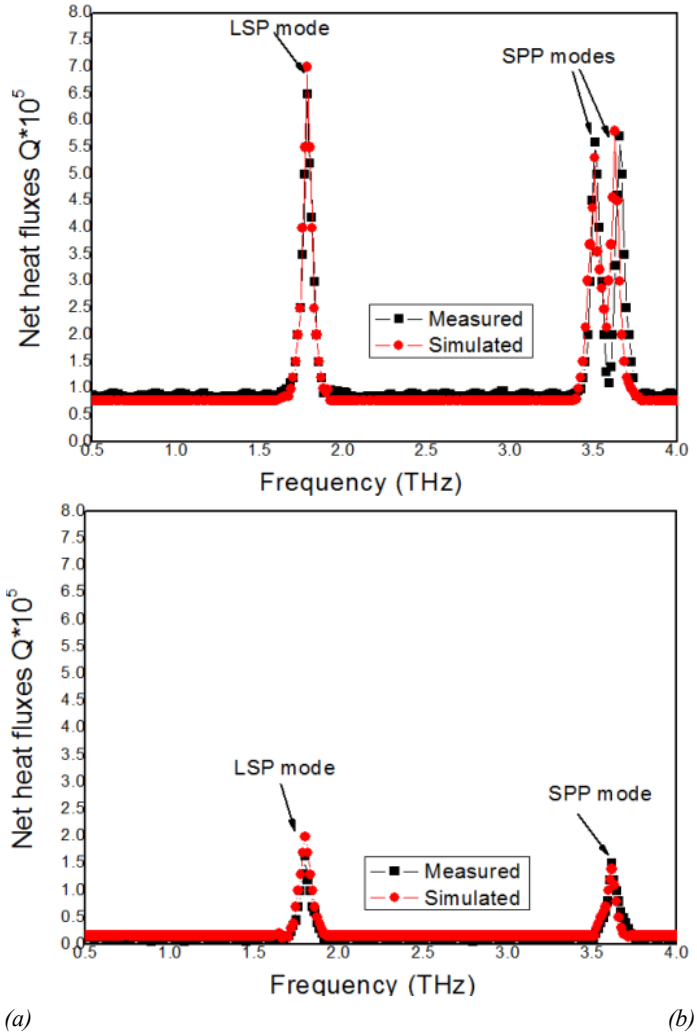

Fig. 2. (a)The measured and simulated results of the proposed metamaterial samples (n=0.55, f=0.03). (b)The measured and simulated results without gradient nanoparticles (colour online)

3. Results

To reveal the relationship between the radiation properties of gradient nanoparticles and metamaterial samples, simulated near-field radiation heat transfer of the metamaterial was obtained. Fig. 3 (a-b) shows the simulated near-field radiation heat transfer of the metamaterial without the use of gradient nanoparticles. The simulation results show that at the resonance point 1.782THz, the LSP mode is excited at the edge of the disk array, as shown in Fig. 3 (a). At the resonance point 3.621THz, the SPP mode is effectively excited within SU-8. These simulation results imply that the LSP mode and the SPP mode are the main factors that excite the radiation peak. Fig. 3 (c-d) shows the simulated near-field radiation heat transfer of the metamaterial under the condition of using gradient nanoparticles. At the resonance point 1.784THz, the LSP mode on the surface of the gradient nanoparticles was effectively excited and coupled with the LSP mode at the edge of the disk array, thereby enhancing the near-field radiation intensity of this metamateral-like sample, as shown in Fig. 3 (c). At the resonance point of 3.626THz, the SPP-LSP coupling effect was also effectively excited, thereby enhancing the near-field radiation performance of the sample. The simulation results in Fig. 3 reveal the enhancement effect of nanogradient particles on the near-field radiation performance of this metamaterial sample. During the process of electromagnetic waves penetrating this metamaterial, the LSP mode on the surface of gradient nanoparticles is excited by electromagnetic waves. These new LSP modes are coupled with the LSP mode at the edge of the disk array or the SPP mode within the SU-8 layer. These LSP-LSP or LSP-SPP coupling effects improve the impedance matching conditions of metamaterial samples near the resonance point, thereby enhancing the corresponding near-field radiation performance. In addition, the filling factor and gradient factor of gradient nanoparticles are tunable parameters. This means that under the condition of using gradient nanoparticles, the near-field radiation properties of this metamaterial sample can be controlled by optimizing the filling factor or gradient factor. Such tunability is conducive to expanding the industrial application fields of this metamaterial sample.

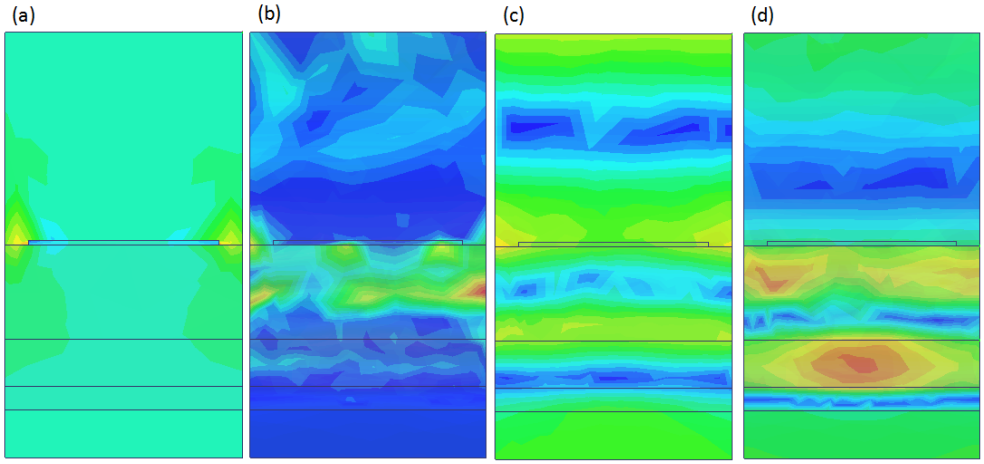

Fig. 3. (a) The simulated near-field strength at 1.782THz without gradient nanoparticles. (b) The simulated near-field radiation heat transfer of the metamaterial at 3.633THz without gradient nanoparticles. (c)The simulated near-field strength at 1.782THz with gradient nanoparticles (d) T The simulated near-field radiation heat transfer of the metamaterial at 3.633THz with gradient nanoparticles (colour online)

Based on the measurement results in Figs. 2 and 3, it can be known that gradient nanoparticles play an important role in improving the near-field radiation performance. In the following experiments, the parameters of the gradient nanoparticles were optimized respectively. In the third group of experiments, the gradient factor of the gradient nanoparticles was optimized (the filling factor remained unchanged), increasing from 0.55 to 0.95. The measurement results of the near-field radiation performance are shown in Fig. 4 (a). As the gradient factor is gradually increased, the LSP peak is gradually strengthened and moved to the low-frequency region. In addition, the two radiation peaks based on the SPP mode have also been gradually strengthened. It should be noted that the two SPP peaks gradually approach each other as the gradient factor increases. When the gradient factor n=0.95, the two SPP peaks are merged into one radiation band. In the fourth group of experiments, the gradient factor was maintained at 0.95, and the fill factor was gradually increased, as shown in Fig. 4 (b). When the fill factor is increased to 0.07, the intensity of the LSP peak is increased to 9.56, and the resonance position is moved to 0.612THz. In addition, as the fill factor is increased, the radiation band is gradually strengthened, with an intensity reaching 0.865 and the central position being 2.423THz.

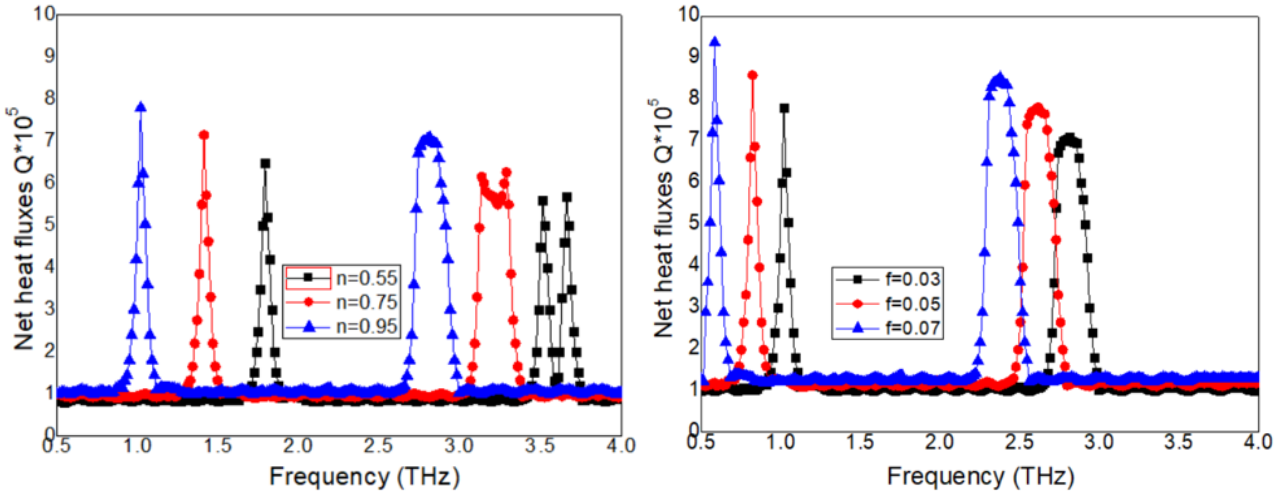

(a) *(b)*

Fig. 4. The measured near-field radiation (a) n is increased with f=0.03 (b) f is increased with n=0.95 (colour online)

The measurement results in Fig. 4 verify the enhancement effect of the gradient factor and the fill factor on the radiation performance, especially the transformation of the radiation peak into a radiation band. Therefore, for industrial application purposes, the near-field radiation performance of metamaterial samples can be controlled by gradient factors and filling factors.

The simulation results in Fig. 5 visually demonstrate the improvement effect of the increase in the gradient factor on the near-field radiation performance of this metamaterial structure. When n=0.95, the LSP mode on the surface of the gradient nanoparticles within the SU-8 layer is strengthened, thereby resulting in the synchronous strengthening of the coupling between these gradient nanoparticles and the edge of the disk array. Therefore, at the resonance point of 1.08THz, the intensity of the LSP peak is increased to 7.945, as shown in Fig. 5 (a). Meanwhile, the original SPP peaks were merged into radiation bands. When n=0.95, the SPP mode within the SU-8 layer is strengthened, as shown in Fig. 5 (b). At the resonance point of 2.806THz, the intensity of thermal radiation reached 7.46. The simulation results in Fig. 5 visually demonstrate the strengthening effect of the gradient factor on the resonance mode.

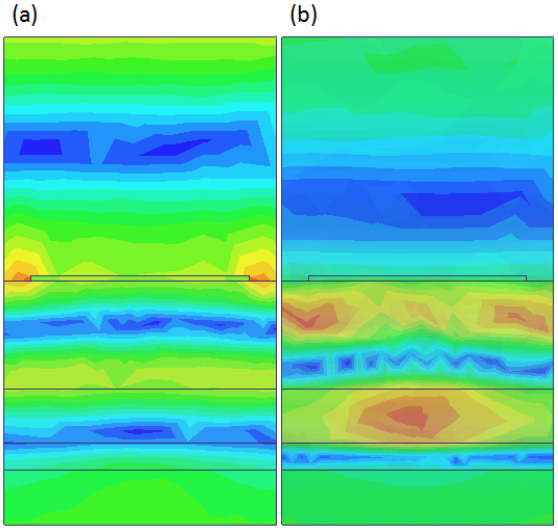

Fig. 5. The near-field radiation strength. (a) At 1.08THz. *(b) At* 2.806THz *(colour online)*

In the fourth group of experiments, the gradient factor was maintained at n=0.95, while the fill factor was increased from 0.03 to 0.07. The near-field radiation performance of this metamaterial sample exhibits two characteristics: on the one hand, both the LSP peak and the radiation band are continuously strengthened. On the other hand, the frequencies of these resonances are all gradually reduced. Fig. 6 shows the intensity distribution of two resonance points under the condition of f=0.07 (n=0.95). At the resonance point of 0.583THz, the LSP patterns at the edge of the disk and on the surface of the gradient nanoparticles were both strengthened, as shown in Fig. 6 (a). The strong LSP-LSP mode coupling effect resulted in the near-field radiation intensity of this metamaterial sample being 0.943. At the resonance point 2.453THz, the SPP mode and the LSP mode on the surface of the gradient nanoparticles are also strengthened, as shown in Fig. 6 (b). The LSP-SPP mode coupling effect excites more intense near-field radiation. Therefore, increasing the filling factor of gradient nanoparticles is an effective method to enhance the near-field radiation performance.

The near-field radiation characteristics of this metamaterial sample are shown in Fig. 4. The performance of NFRHT is an important factor affecting photoelectric equipment. At present, photoelectric devices based on NFRHT performance have been frequently reported and applied by researchers [19-22]. However, metamaterials based on gradient nanoparticles have not yet received attention from researchers in the field of thermal conductivity sensing for fabric samples. Here, the metamaterial sample is applied to the thermal conductivity sensing scheme of fabric samples. This is a high-performance NFRHT based on the metamaterial sample, as shown in Fig. 5. The measurement results verified the effectiveness of this sensing scheme, thereby providing a foundation for expanding the application fields of metamaterials. The specific measurement method is as follows: (a) Clean the surface of the aluminum plate with ultrapure water and dry the surface with a hot plate. (b) Lay the fabric sample to be measured flat on the surface of the aluminum plate and squeeze it to achieve effective contact. (c) Place the metamaterial sensor on the surface of the fabric sample (with a thickness of 1.0mm, Silk fabric). (d) Connect a low

voltage DC power supply to the metamaterial and aluminum plate to obtain a stable electric field. (e) Use a hot plate to form thermal pulses and successively penetrate the metamaterial and fabric samples to reach the surface of the aluminum plate. (f) When the thermal pulse reaches the surface of the aluminum plate, it will excite the corresponding thermal pulse current. Use a transistor amplification circuit to obtain these thermal pulse currents and display them with an oscilloscope. When the thickness of the fabric sample is 1.0mm, the measured thermal pulse current is shown by the black curve in Fig. 7 (a).

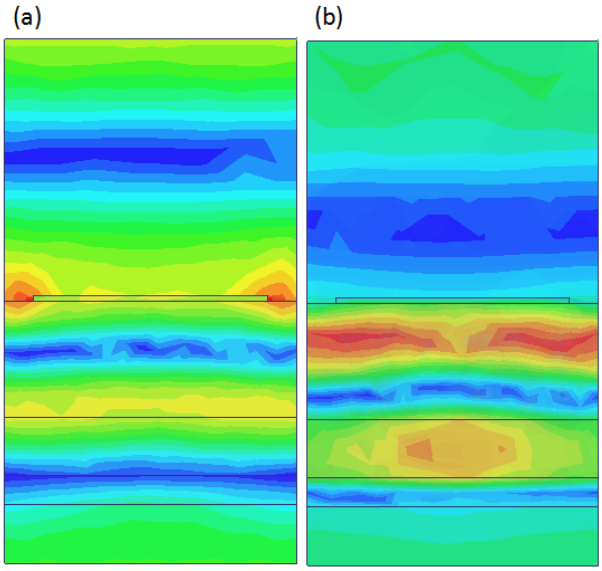

Fig. 6. The near-field radiation strength. (a) at 0.583THz. *(b) at* 2.453THz *(colour online)*

The thermal pulse current exhibits three fundamental characteristics: in the early stage of the experiment, within 0 to 0.85 seconds, the intensity of the thermal pulse current is very low. This is because the thermal pulse excited by the hot plate needs to consume 0.85 seconds to successively penetrate the metamaterial and fabric samples before reaching the surface of the aluminum plate. These thermal pulses cannot heat the localized surface of the aluminum plate to a strength sufficient to cause deformation within 0.85 seconds. Therefore, within the range of 0 to 0.85 seconds, the intensity of the thermal pulse current is very low. In the middle of the experiment, within 0.85s-1.93s, the intensity of the thermal pulse current was rapidly enhanced to 9.34. This is because the thermal pulse reaching the aluminum plate forms sufficient thermal deformation on the local surface, thereby exciting the corresponding thermal pulse current and obtaining it by the amplification circuit. In the later stage of the experiment, when the measurement time exceeded 1.93 seconds, the intensity of the thermal pulse current was gradually stabilized at 9.42. This is because the thermal pulse intensity of the aluminum plate has tended to stabilize, thereby stimulating a stable thermal pulse current. The measured thermal pulse currents verified the effectiveness of the sensing scheme. In the fifth group of experiments, the thickness of the fabric samples was gradually increased, from 1.0mm to 1.3mm. The measurement results of the thermal pulse current are presented in Fig. 7 (a). As the thickness of the fabric sample increases, the measurement results of the thermal pulse current exhibit two fundamental characteristics: on the one hand, the time for the thermal pulse current to reach its peak is prolonged. On the other hand, the peak value of the thermal pulse current is gradually weakened, as shown in Fig. 7 (a). When the thickness of the fabric sample is increased, the time it takes for the same thermal pulse to penetrate the fabric sample will be prolonged. This leads to an increase in heat loss. Therefore, the time required to excite the corresponding thermal pulse current on the surface of the aluminum plate will be synchronously prolonged. In addition, as the intensity of the thermal pulse reaching the surface of the aluminum plate gradually decreases with the increase of the thickness of the fabric sample, the intensity of the thermal pulse current obtained by the amplification circuit also decreases synchronously, as shown in Fig. 7 (a). These measurement results reveal the direct effect of the thickness of fabric samples on thermal conductivity. Meanwhile, based on the thermal pulse current obtained in Fig. 7 (a), the thermal conductivity coefficient and thermal resistance of the fabric sample can also be extracted simultaneously:

$$I(t) = \frac{A}{d}\int_o^d g(y)\frac{\partial \Delta\theta(y,t)}{\partial t}dy \tag{1}$$

$$g(y) = (a_\varepsilon - a_y)\varepsilon_o\varepsilon_r E(y) + P_{Xuan-paper}(y) \quad (2)$$

$$P_{Xuan-paper} = P_{All-structures} - P_{Ambient} \quad (3)$$

$$R_{\text{Overall}} = R_{sensor} + R_{Xuan-paper} + R_{Substrate} \quad (4)$$

According to the intensity of the thermal pulse current in Fig. 7 (a), the thermal resistances of fabric samples of different thicknesses are: 19.4, 20.5, 21.8, 23.1, 24.5, and the thermal conductivity coefficients are: 8.22, 7.16, 6.21, 5.34, 4.56.

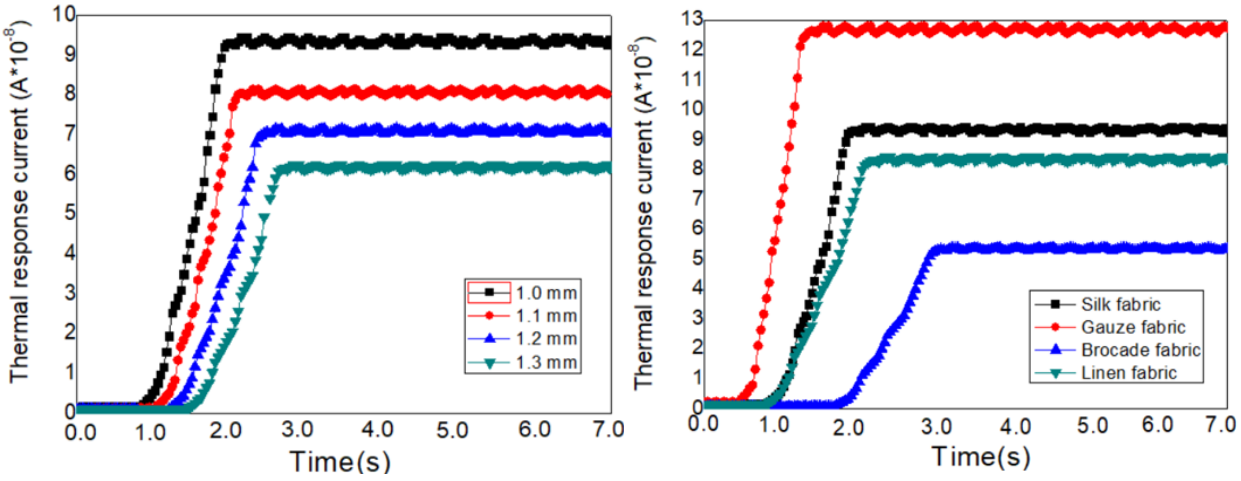

(a) *(b)*

Fig. 7. (a) Thermal currents under different thicknesses. (b) Thermal currents with different fabric samples (colour online)

In the last set of experiments, four fabric samples were measured based on the same method, and the thermal pulse current is shown in Fig. 7 (b). Among them, the intensity of the thermal pulse current of the Gauze fabric sample is the highest and the required time is the shortest, as shown by the red curve. The intensity of the thermal pulse current of the Brocade fabric sample is the lowest and the required time is the longest, as shown by the blue curve. The thermal resistances of these fabric samples are: 19.4, 15.3, 26.1, 21.1, and the thermal conductivity coefficients are: 8.22, 13.14, 4.86, 7.85. These measurement results reveal the significant influence of fabric types on thermal conductivity. Such differences are mainly based on the variations in the composition of fabric samples and the preparation processes. The measurement results shown in Fig. 7 verify that the proposed metamaterial sensing scheme is effective. These measurement results provide a foundation for expanding the application fields of metamaterials.

4. Conclusion

The NFRHT characteristics of functional devices have attracted the attention of researchers. Here, a metamaterial with multimodal resonance is proposed and measured. The near-field radiation peaks based on the LSP mode and the SPP mode were obtained. The near-field radiation performance of this metamaterial sample can be controlled by optimizing the filling factor and gradient factor of the gradient nanoparticles. A sensing scheme based on this metamaterial sample was proposed and applied to measure the thermal conductivity of fabric samples (including thermal pulse current, thermal resistance, and thermal conductivity coefficient). The relationship between the thickness and type of fabric samples and their thermal conductivity has been revealed. These measurement results verified the effectiveness of the metamaterial sensing scheme and provided a foundation for expanding the application of metamaterials.

Declaration of interests

The authors declare that they have no known competing financial interests or personal relationships that could have appeared to influence the work reported in this paper.

Acknowledgments

This research was financially supported by Young and Middle Teachers' Basic Ability Improvement Project of Guangxi (No. KY2016YB453).

References

[1] Z. Song, K. Wang, J. Li Q.H. Liu, Opt. Express **26**, 7148 (2018).

[2] Y. I. Abdulkarim, L. W. Deng, M. Karaaslan, E. Unal, Chem. Phys. Lett. **732**, 136655 (2019).

[3] Q. Wang, E. Plum, Q. Yang, X. Zhang, Q. Xu, Y. Xu, J. Han, W. Zhang, Light: Science and Applications **7**, 25 (2018).

[4] Z. C. Guo, K. H. Wen, Q. Y. Hu, W. H. Lai, J. Y. Lin, Y. H. Fang, Sensors **18**, 1348 (2018).

[5] P. Qi, Y. Luo, B. Shi, W. Li, D. Liu, L. Zheng, Z. Liu, Y. Hou, Z. Fang, eLight **1**, 6 (2021).

[6] D. Lee, S. So, H. Guangwei, M. Kim, T. Badloe, H. Cho, J. Kim, H. Kim, C.-W. Qiu, J. Rho, eLight **2**, 1 (2022).

[7] M. Esen, İlhami İlhan, R. E. Karaaslan, Ramazan Esen, Applied Nanoscience **10**, 551 (2020).

[8] M. Ozturk, O. Akgol, U. K. Sevim, M. Karaaslan, M. Demirci, E. Unal, Constr. Build. Mater. **165**, 58 (2018)

[9] J.-H. Deng, H. Xiong, Q. Yang, M. Suo, J.-Y. Xie, H.-Q. Zhang, IEEE Sensors Journal **23**(19), 22459 (2023).

[10] B. X. Wang, G. Duan, W. Lv, Y. Tao, D. Z. Hong, G. Yang, F. Z. Shu, Nanoscale **45**, 18435 (2023).

[11] B.-X. Wang, X. Qin, G. Duan, G. Yang, W.-Q. Huang, Z. Huang, Adv. Funct. Mater. **34**(224), 2402068 (2024).

[12] X. Qin, S. Fang, G. Duan, X. Chongyang, J. Jiang, H. Xiong, B.-X. Wang, Nanoscale **16**(34), 16238 (2024).

[13] Pu. Jepsen, B. M. Fischer, A. Thoman, H. Helm, Phys. Rev. B. **74**, 205103 (2006).

[14] Q. Y. Wen, H. W. Zhang, Q. H. Yang, Y. S. Xie, K. Chen, Y. L. Liu, Appl. Phys. Lett. **97**, 021111 (2010).

[15] Y. H. Zhu, S. H. Vegesna, Y. Zhao, V. Kuryatkov, M. Holtz, Z. Y. Fan, M. Saed, A. A. Bernussi, Opt. Lett. **38**, 2382 (2013).

[16] K. H. Park, J. H. Shin, H. C. Ryu, Nanotechnology **27**, 195202 (2016).

[17] P. Ben-Abdallah, K. Joulain, J. Drevillon, G. Domingues, J. Appl. Phys. **106**, 044306 (2009).

[18] J. C. Cuevas, F. J. García-Vidal, ACS Photonics **5**, 3896 (2018).

[19] Y. Yang, B. Li, Y. Hu, H. Wang, X. Tang, L. Wang, Y. Zhu, Int. J. Heat Mass Transf. **191**, 122824 (2022).

[20] D. Feng, S. K. Yee, Z.M. Zhang, Appl. Phys. Lett. **119**, 181111 (2021).

[21] F. Chen, X. Liu, Y. Tian, Y. Liu, Y. Zheng, Appl. Phys. Lett. **119**, 221107 (2021).

[22] O. R. Toyin, W. Ge, L. Gao, Chin. Phys. Lett. **38**, 016801 (2021).

[23] Y. X. Li, Y. D. Dang, S. Zhang, X. R. Li, T. L. Chen, P. K. Choudhury, Y. Jin, J. B. Xu, P. Ben-Abdallah, B. F. Ju, Y. G. Ma, Nature Communications **15**, 5465 (2024).

[24] N. Iqbal, S. Zhang, P. K. Choudhury, Y. Jin, Y. G. Ma, International Journal of Thermal Sciences **172**, 107315 (2022).

[25] S. Zhang, Y. D. Dang, X. R. Li, I. Naeem, Y. Jin, P. K. Choudhury, M. Antezza, J. B. Xu, Y. G. Ma, Physical Review Applied **21**, 024054 (2024).

[26] S. Zhang, Y. D. Dang, X. R. Li, Y. X. Li, Y. Jin, P. K. Choudhury, J. B. Xu, Y. G. Ma, Nanoscale **16**, 1167 (2024).

[27] S. A. Dyakov, J. Dai, M. Yan, M. Qiu, Journal of Physics: Applied Physics **48**, 305104 (2015).

[28] S. G. Castillo-López, A. Márquez, R. Esquivel-Sirvent, Phys. Rev. B **105**, 155404 (2022).

[29] M. Q. Liu, C. Y. Zhao, Int. J. Heat Mass Transf. **186**, 122435 (2022).

[30] C. L. Zhou, G. Tang, Y. Zhang, M. Antezza, H. L. Yi, Phys. Rev. B **106**, 155404 (2022).

*Corresponding author: zhongmin2012hy@163.com